13th International Symposium on Particle Image Velocimetry – ISPIV 2019
Munich, Germany, July 22-24, 2019

PIV measurements of hypersonic laminar flow over a compression ramp

Jin Lu[1], Hua Yang[1*], Qinghu Zhang[2], Zhouping Yin[1]

[1] Huazhong University of Science and Technology, State Key Laboratory of Digital Manufacturing Equipment and Technology, Wuhan, China

[2] China Aerodynamics Research and Development Center, Hypervelocity Aerodynamics Institute, Mianyang, China

[*] huayang@hust.edu.cn

Abstract

Experimental investigations of hypersonic laminar flow over a compression ramp are carried out in a Mach 5.0 wind tunnel, and the angles of the ramp are 32°, 36° and 40°. High-spatial-resolution images of the laminar inflow over the three different compression ramps are captured. The fine structures of the holistic flow field and local regions are measured by the particle image velocimetry (PIV) technique, and some typical flow structures, such as the boundary layer, shear layer, separation shock, recirculation zone and reattachment shock, are clearly visible. The locations of the separation shock and reattachment shock and the development of the boundary layer after reattachment are measured by time-averaged flow field structures. The proper orthogonal decomposition (POD) analysis of the velocity fields is performed for three cases and reveals the spatial structure characteristics of the flow field. The experimental results indicate that when the ramp angle is 32°, the hypersonic laminar flow does not show separation, and the boundary layer always adheres to the ramp. When the ramp angle increases to 36°, the typical separation appearing in hypersonic laminar flow with boundary layer increases and is converted into turbulence quickly; at the same time, a shock is induced by the developing boundary layer, and shear layer and compression waves arise in the flow field. When the ramp angle is 40°, the range of the recirculation zone expands obviously in the hypersonic laminar flow which is separated further, the separation shock moves upstream and the reattachment shock moves downstream.

1 Introduction

As a typical aerodynamic configuration, compression ramps commonly appear on the surface of hypersonic aircraft. Under hypersonic flow, the flow separation and shock wave boundary layer interaction caused by the compression ramp form complex flow field structures and unsteady dynamics characteristics on the aircraft surface, seriously affecting the performance of the aircraft and propulsion system (Hadjadj and Dussauge, 2009). The resulting large-scale low-frequency motions of the shock wave cause the aircraft surface pressure to oscillate, eventually causing chattering and stalling of the aircraft (Agostini et al., 2015). At the same time, the interaction between the shock wave and the boundary layer leads to the unsteady separation of the boundary layer on the aircraft wall, which induces high-frequency pulsation of the aerodynamic force, surface heat flow and pressure load. This effect can produce unpredictable aerodynamic forces and aerodynamic moments that seriously affect the effective control of the aircraft (John and Kulkarni, 2014; Gaitonde, 2015). In addition, the unsteady separation of the boundary layer on the aircraft wall caused by the shock wave boundary layer interaction is an important source of aerodynamic resistance of the aircraft. These aspects undoubtedly pose serious challenges to the aerodynamic shape design, drag reduction and structural optimization of the aircraft. Therefore, analyzing these complex flow phenomena and revealing their mechanism of action is related not only to component design and performance estimation for hypersonic vehicles but also to the prediction of the overall machine performance (Gaitonde, 2013).

Many numerical simulations and experimental measurements of the flow field structures in the compression ramp flow have been studied because of its importance to the aerodynamic configuration design of hypersonic aircraft. Edwards et al. (2008) numerically calculated the compression ramp flow and analyzed

the average flow structure of the separation zone and found that the continuous convergence of the wave system caused the vibration of the separation surface. Wu and Martin (2008) calculated the compression ramp flow structure at 2.9 Mach by direct numerical simulation and found that the motion of the separation shock has no significant effect on the characteristics of the upstream boundary layer. The correlation between the separation point, the reattachment point, and the position of the separation shock indicated that the vibration of the shock wave is affected by the downstream flow. Ganapathisubramani et al. (2007) used planar laser scattering (PLS) technique to obtain the extended flow structure of compression ramps at different normal heights at 2 Mach and found that there are strip-like quasi-order structures with uniform dynamics and spacing distribution in the upstream boundary layer. Ganapathisubramani et al. (2006) measured the velocity field structure of a 20° compression ramp at 2 Mach and found that the location of the separation zone is closely related to the velocity of the upstream boundary layer. Schreyer et al. (2011) studied the velocity field structure of a 33° compression ramp at hypersonic speed and found that the shock wave has relatively little influence on the turbulence intensity of the flow direction, and the influence on the normal turbulence intensity is more significant. Helmer et al. (2012) measured the velocity field of a 20° compression ramp in spanwise planes and found that there is a significant difference between the shock angle and the boundary layer velocity profile at different planes. Numerical simulations have made great progress and have performed well in many studies. However, the complex flow field structure in the compression ramp imposes higher requirements on the accuracy of the calculation model, which makes the numerical simulation currently unable to give very satisfactory results. Experimental measurements are still the primary means of studying the compression ramp flow. However, complex flow field structures require measurement techniques with high temporal and spatial resolution to accurately capture the flow structures. Although numerical simulation and experimental research in the field of fluid mechanics have been greatly improved, some physical mechanisms in the compression ramp flow have not been uniformly understood, especially in the case of hypersonic flow.

Particle image velocimetry (PIV) is a new flow measurement technology developed on the basis of flow field display technology using advanced image processing technology (Zhong et al., 2017). PIV combines the advantages of single-point measurement and flow display technology, it has high accuracy and high resolution, and could obtain the overall structure and transient image of the planar flow field. Because of the advantages of nonintrusive and full-field measurements, PIV has been widely used in hydrodynamics, aerodynamics and many other experimental studies (Lee et al., 2017b). The principle of PIV technology is to spread the tracer particles evenly in the flow field and record two images at short intervals through the camera. The particle velocity is determined by calculating the particle image pairs, and the velocity is used as the velocity of the fluid to obtain the flow parameters of the whole field. PIV has evolved to be the dominant method for velocimetry in experimental fluid mechanics and has contributed to many advances in our understanding of hypersonic flows (Lee et al., 2017a). The implementation of PIV with nanometric seeding particles and microsecond pulse separation allows the measurement of the instantaneous planar velocity field over a two-dimensional compression ramp in a Mach 5 free stream flow.

Proper orthogonal decomposition (POD) is an unbiased method for extracting structural information by decomposing eigenfunctions by the Karhunen-Loeve method, and its physical essence is to decompose random fields into basic modalities (Sieber et al., 2016). Due to the optimality of the choice of function basis, the first few expansions of POD can often approximate the original signal. Therefore, POD has been widely used in the fields of image processing, process identification, data reconstruction and random variable analysis (Chatterjee, 2000). POD was proposed as an unbiased method for extracting structures in a turbulent flow and has proven to be an effective method for identifying the dominant structures in both experimental and numerical data (Rowley, 2005). When POD is applied to velocity fluctuation data, the modes represent the turbulent kinetic energy. Almost all previous experimental studies of POD were applied to low-velocity flow, and the experimental results of POD for hypersonic flow were rarely reported(Podvin and Fraigneau, 2017).

In summary, due to the interaction of the shock wave with the boundary layer and the interaction of the shock wave with itself, the flow field of the compression ramp includes complex flow field structures such as separation, shearing and reattachment. This condition may cause high-frequency pulsations of the aircraft's aerodynamic forces, surface heat flow and pressure loads in addition to structural damage to the aircraft. This aircraft problem should not be neglected in design, so the flow field structure of the compression ramp is a focus of researchers' attention. Hence, the aims of this research project are to measure the velocity fields of hypersonic laminar flow over compression ramps by PIV and analyze the effects of different ramp angles on the flow separation. The rest of the present paper is organized as follows. In section 2, the flow facility and PIV technique are described in detail. Experimental results, including the flow imaging, velocity profiles, and POD of the velocity, are given in section 3. Conclusions drawn from the present work are summarized in section 4.

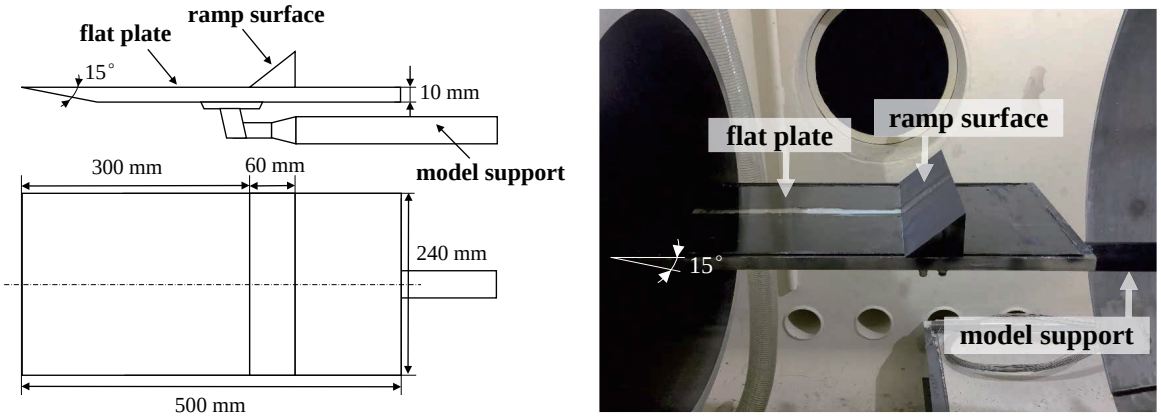

(a) Schematic of the compression ramp model (b) Compression ramp model placed inside the test section

Figure 1: The details of the two-dimensional compression ramp model.

2 Experimental setup

2.1 Flow facility and compression ramp model

The experiments were performed in the hypersonic wind tunnel facility at China Aerodynamics Research and Development Center (CARDC), which is a conventional high-pressure-blow and vacuum-suction hypersonic wind tunnel with a test-section diameter of 500 *mm* and a variable Mach number capability over the range of Mach $5 \sim 10$ with maximum run time of 360 *s*. The wind tunnel facility consists of a gas source system, a heater, a reversing valve, a bypass system, a stabilizing section, a nozzle, a test section, a diffuser section, a cooler, a vacuum system, and a measurement and control system. The flight height range that can be simulated by the wind tunnel facility is 20 $km \sim 60$ *km*, the Reynolds number range is $5.93 \times 10^5 \sim 5.89 \times 10^7/m$, the total temperature range is 288 $K \sim 1081.76$ *K*, and the total pressure range is 0.15 $MPa \sim 12$ *MPa*. The experiments were performed with a Mach number of 5, and the total temperature and total pressure were 350 *K* and 0.5 *MPa*, respectively.

The compression ramp model was fabricated in aluminum on a computer numerical control (CNC) machine with an accuracy of 0.01 *mm*. Thereafter, the model surface was polished to obtain a mean roughness of 0.5 μm, as shown in Fig. 1(a). The length of the flat plate was 500 *mm*, the length of the ramp was 60 *mm*, the spanwise width of the model was 240 *mm*, and the distance from the plate-ramp junction to the front edge of the flat plate was 300 *mm*. The choice of a 32° to 40° compression ramp model was made primarily due to its large separated region, making it easier to demonstrate the feasibility of the detection system to capture the flow details. The test model was mounted on a support pipe along the test-section centerline. The model was located in the main flow area, and a laminar boundary layer was formed on the surface by hypersonic flow, as shown in Fig. 1(b). A transparent glass was placed in the middle of the model to allow the laser to pass through the model to prevent strong reflections on the surface of the model. The spanwise width of the model was long enough to enable the flow to be considered two dimensional.

2.2 PIV technique

As shown in Figure 2, the two-dimensional PIV system is composed of a light source, a synchronous controller, imaging and processing systems, and a nanoparticle generator. A dual-cavity Nd:YAG-pulsed laser that emits two laser beams of 532 *nm* wavelength with a maximum energy of 430 *mJ* and a frequency of 10 *Hz* and pulse width of 60 *ns* is used as the light source, and a laser sheet less than 0.2 *mm* thick illuminates the region of interest. A PowerView Plus 4MP-HS camera with a resolution of 2048 $pixels \times 2048$ *pixels* is used to record a flow field of 100 $mm \times 100$ *mm* with a pulse delay of 0.5 μs. A synchronizer with an accuracy of 0.25 *ns* ensures that the laser and the CCD work simultaneously. The computer is in charge of sending instructions and storing and processing images. The image data are analyzed after each run with a cross-correlation technique using the TSI Insight4.0 software. The initial correlation interrogation window size is set to 32 $pixels \times 32$ *pixels*, and the final correlation interrogation window size is set to 16 $pixels \times 16$ *pixels* with 50% overlap shifting during the analysis. With these settings, the percent of

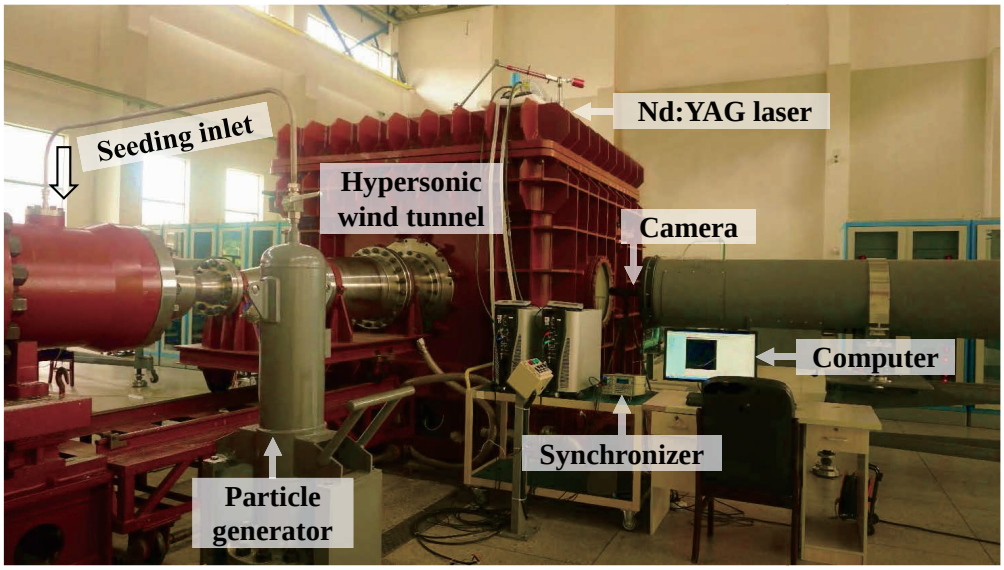

Figure 2: PIV technique setup.

valid vectors is in the range of $95 \sim 98\%$. Because timing errors of the Nd:YAG laser can be excluded, the velocity measurement accuracy depends on the correlation peak estimation error.

TiO_2 particles were used to seed the test gas in the stabilizing section before the experiment was initiated. The nominal particle diameter d given by the supplier was 20 nm, and a scanning electron microscopy analysis yielded a dynamic diameter of approximately 200 nm due to agglomeration. For this diameter, the theoretical particle relaxation time τ was calculated with $\tau = d^2\rho/18\mu$ to 0.41 μs, $\rho = 4230\ kg/m^3$ is the particle density, and $\mu = 2.28 \times 10^{-5}\ kg/(m \cdot s)$ is the dynamic viscosity coefficient at 350 K. The particles were injected simultaneously with the air test gas into the stabilizing section by means of a fluidized-bed seeder. To avoid larger agglomerated TiO_2 particles entering the tube, a cyclone separator controlled the size distribution of the particles, allowing only smaller particles to pass. The seeding density of TiO_2 was optimized by several preliminary experiments, and good results were obtained for a mass ratio (particles/gas) of approximately 0.2%, which corresponded to a theoretical seeding density of approximately $10,000\ particles/mm^3$ in the test section. Approximately $10 \sim 20$ particles were present per interrogation window. However, the particle density varied considerably due to the strong density gradients in the flow.

3 Results and discussion

3.1 PIV-measured velocity profiles

PIV images of hypersonic laminar flow over the three different compression ramps are presented in Figure 3. It can be observed that the Mach 5 hypersonic laminar flow over the compression ramp and turns into turbulent flow in the vicinity of the compression ramp inflection point. The compression ramp causes an oblique shock wave, and the pressure difference before and after the shock causes an adverse pressure gradient in the flow field. As the ramp angle increases, the adverse pressure gradient becomes stronger, and the hypersonic laminar flow passes through different stages, such as boundary layer transition, flow separation and reattachment, throughout the flow process.

The velocity field contours, the streamwise velocity contours and its gradient distributions, the longitudinal velocity contours and its gradient distributions, and the streamlines and the vector fields for the three different compression ramps are presented in Figure 4, Figure 5, and Figure 6. It can be seen from the figures that the flow structures of the hypersonic laminar flow over the three different compression ramps have been successfully captured through the PIV measurements. The trend of the streamlines clearly indicates the separation and reattachment of the flow. The laminar boundary layer produces a typical flow separation under the influence of the adverse pressure gradient. The boundary layer flow is slowed by the separation shock and the reattachment shock, and the direction of the boundary layer flow is changed after separation.

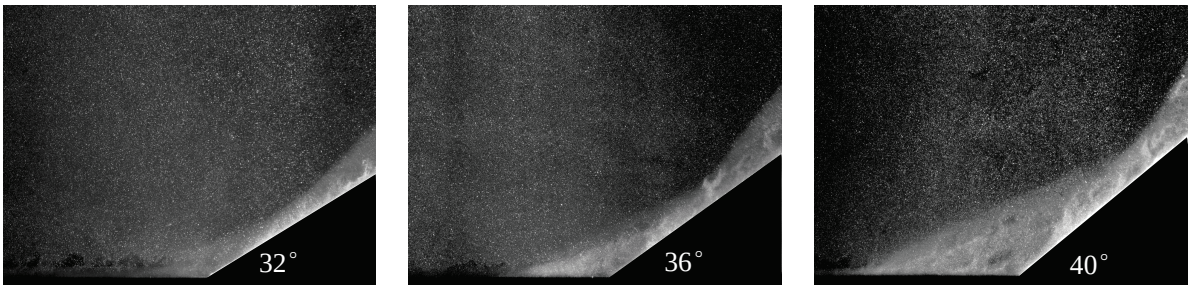

(a) 32° compression ramp (b) 36° compression ramp (c) 40° compression ramp

Figure 3: PIV images of hypersonic laminar flow over three different compression ramps.

The separated boundary layer flows through a series of complex processes whose direction is parallel to the compression ramp at downstream location.

The shear layer gradually forms and grows along the flow direction, and the shear structure and shearing degree also increase. The shear layer surrounds the recirculation zone, and the mainstream velocity outside the shear layer is uniform. The change of the vector fields reflects the velocity shear and gradient change inside the shear layer. However, due to the influence of the flow separation and shearing effect, the velocity direction is deflected and shows a tendency to coincide with the direction of compression of the flow channel. Due to the influence of the flow channel compression, the downstream mainstream flow field produces a longitudinal acceleration under the influence of the disturbance. As the propagation and superposition of the disturbance and the degree of compression of the flow channel increase, the longitudinal velocity further increases, and a region with a large longitudinal velocity appears. Subsequently, the flow is affected by the shock, and the velocity in the longitudinal direction gradually decreases. In areas outside the disturbance zone, the flow is unaffected, and the velocity remains uniform.

It can be seen from the figures that the vicinity of the reattachment point follows the flow structure at the end of the separation zone. The overall trend of the streamline reflects both the recirculation motion in the separation zone and the reattachment of the flow on the compression ramp. The change of the velocity vector indicates that the range of the recirculation zone is gradually reduced. The structure of the mixed layer is increasingly obvious, and close to the compression ramp, the compression wave structure gradually increases and converges on the sloped surface to form a reattachment shock. The range of transition of the shear layer from low-speed to high-speed flow is gradually expanded, and the end of the recirculation zone is the position where the flow is reattached. As the ramp angle increases, the influence of the adverse pressure gradient in the downstream region gradually increases. When the ramp angle increases to 36°, the boundary layer separates and forms a recirculation zone; when the ramp angle increases to 40°, the recirculation zone is expanded. To better highlight the separation shock and reattachment shock, the longitudinal velocity component distributions and gradient distributions are presented as contour plots. It can be seen that as the ramp angle increases, the separation shock moves upstream, the attachment shock moves downstream, and the recirculation zone expands.

3.2 POD analysis

POD is applied to the velocity fields for the three different compression ramps, providing the value of energy in every mode. The idea behind POD analysis is to find a function basis $\phi^n(x)$ that most faithfully represents an instant vector function $f(x)$ in the following form: $f(x) = \sum_{n=1}^{N} a_n \phi^n(x)$, such that the above equation describes $f(x)$ better than any other representation of the same dimension using any other functional basis. Therefore, the relative contribution of turbulent kinetic energy can be given in particular modes. The spectra of the velocity field POD results for the three different compression ramps are shown in Figure 7. Fig. 7(a) shows the relative contribution of the individual POD modes, and Fig. 7(b) shows the cumulative contribution rate.

It can be seen that the first mode for the velocity decomposition results contains a high percentage of the energy. The relative contribution for the 32° compression ramp is 14.9%, whereas the contributions for the 36° compression ramp and 40° compression ramp are 22.9% and 22.1%, respectively. This finding indicates that the ratio of the turbulent kinetic energy for a large compression ramp angle has a larger proportion than that for a small compression ramp angle. The result is that the less deterministic a flow is, the less

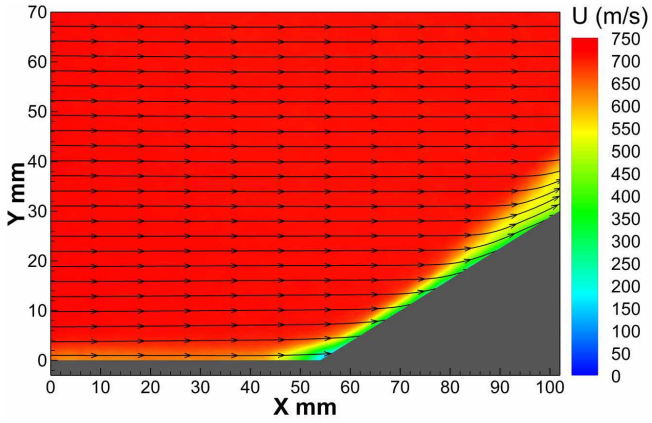

(a) Velocity contours and streamlines

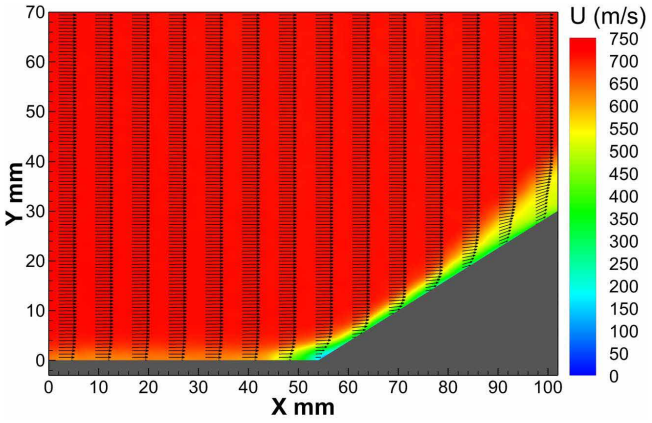

(b) Velocity contours and vector fields

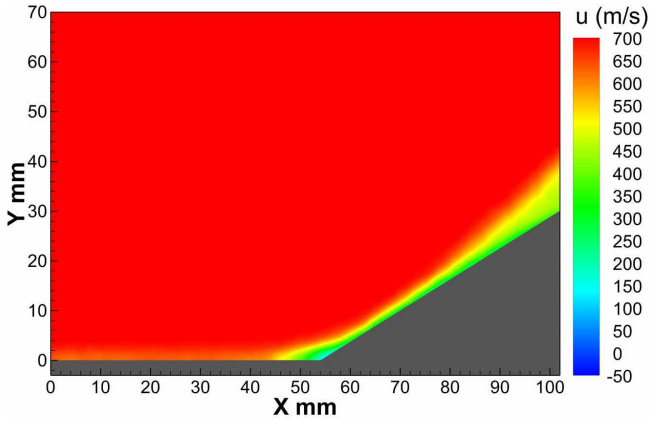

(c) Streamwise velocity contours

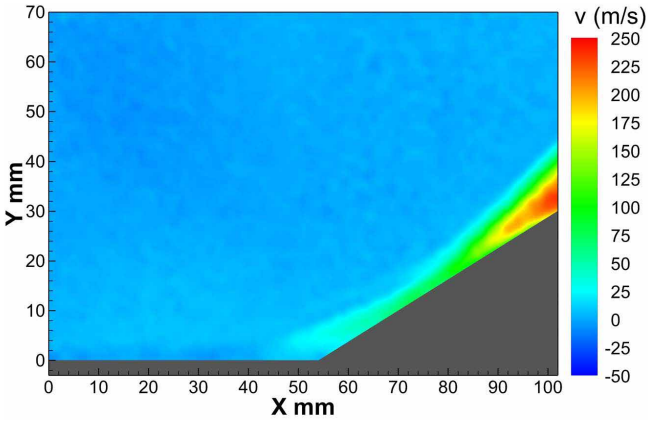

(d) Longitudinal velocity contours

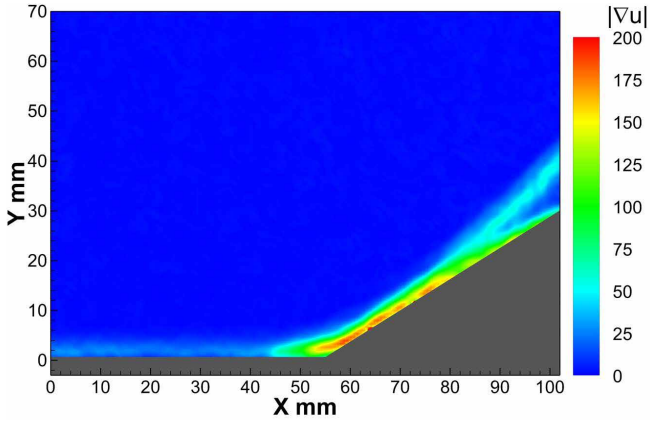

(e) Gradient contours of the streamwise velocity

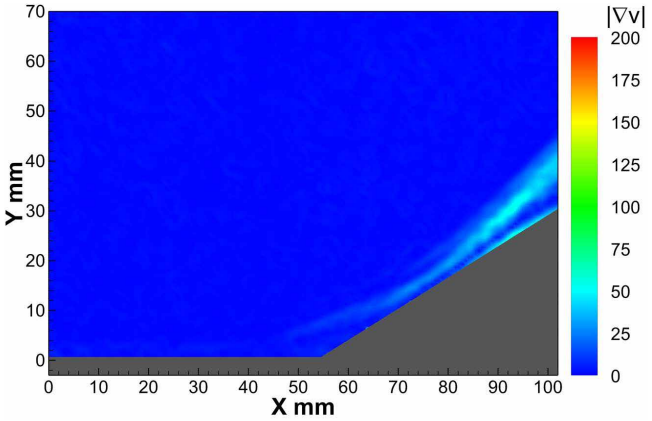

(f) Gradient contours of the longitudinal velocity

Figure 4: PIV measurement results of the 32° compression ramp model.

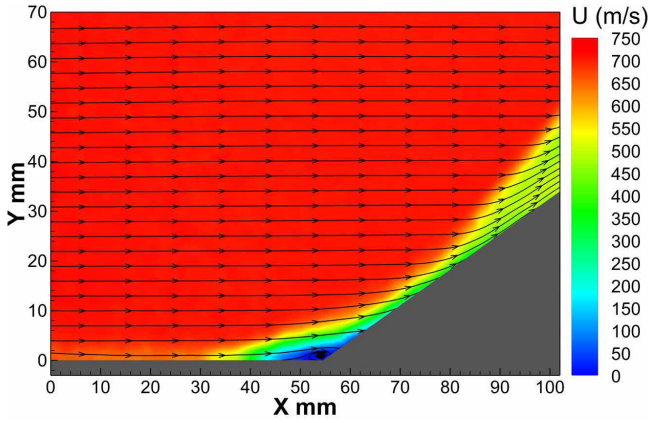

(a) Velocity contours and streamlines

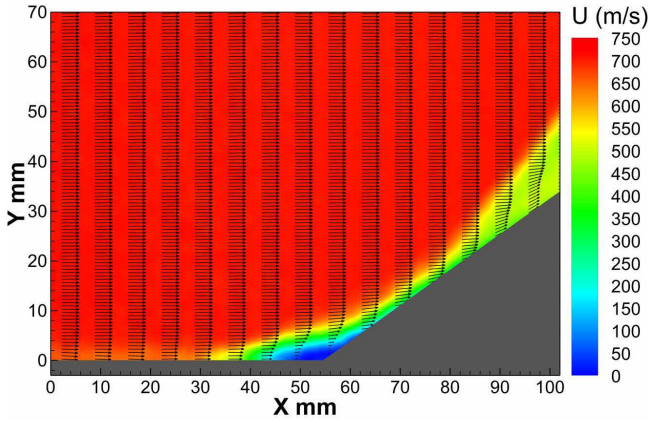

(b) Velocity contours and vector fields

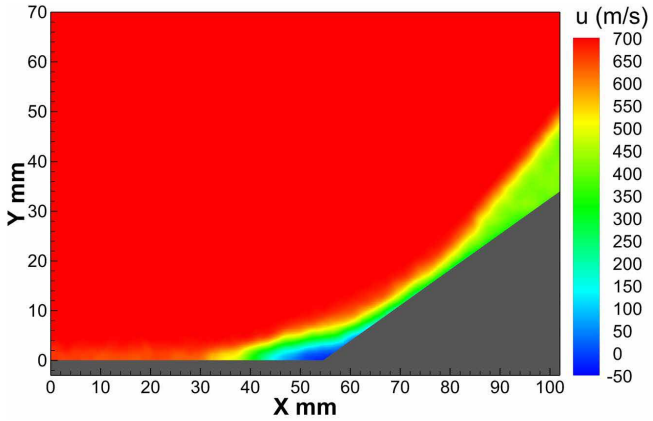

(c) Streamwise velocity contours

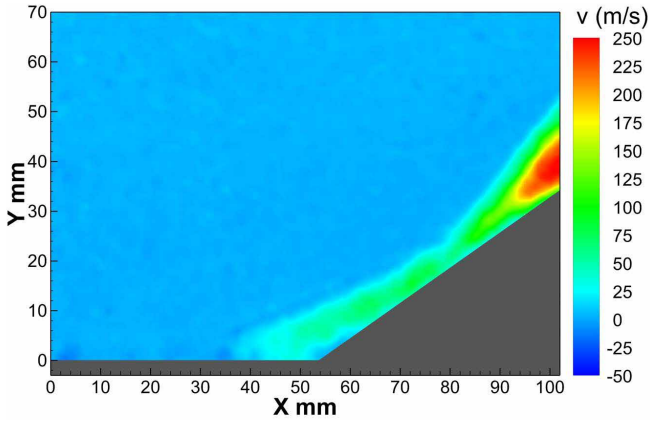

(d) Longitudinal velocity contours

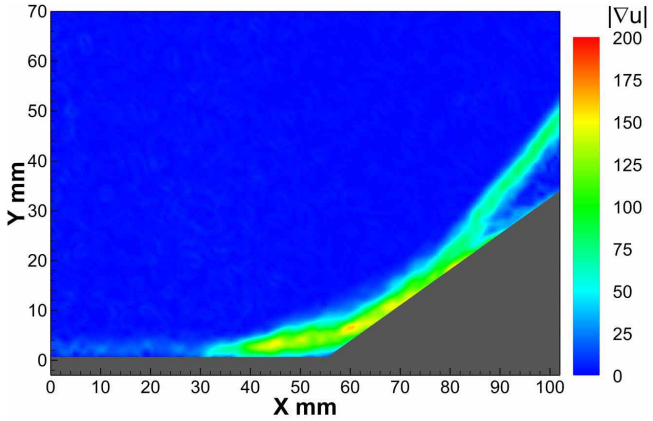

(e) Gradient contours of the streamwise velocity

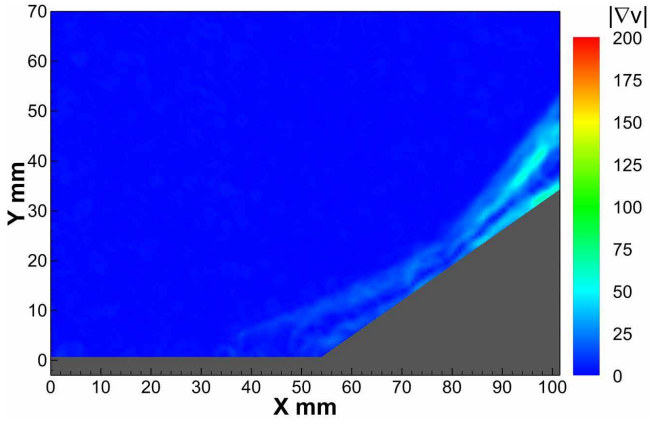

(f) Gradient contours of the longitudinal velocity

Figure 5: PIV measurement results of the 36° compression ramp model.

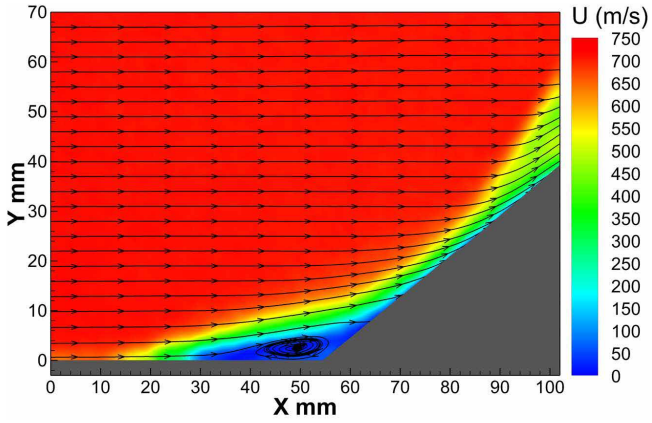

(a) Velocity contours and streamlines

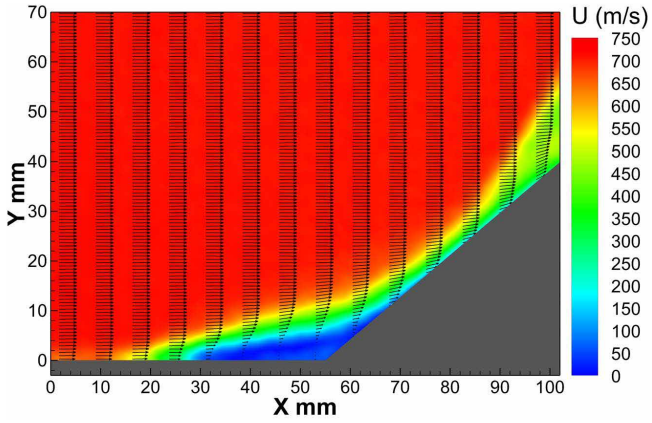

(b) Velocity contours and vector fields

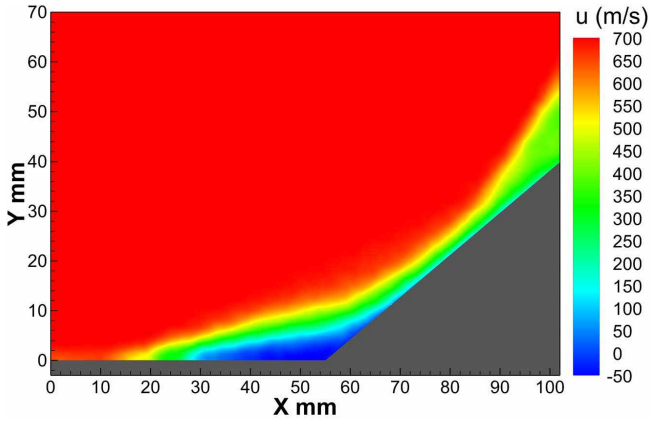

(c) Streamwise velocity contours

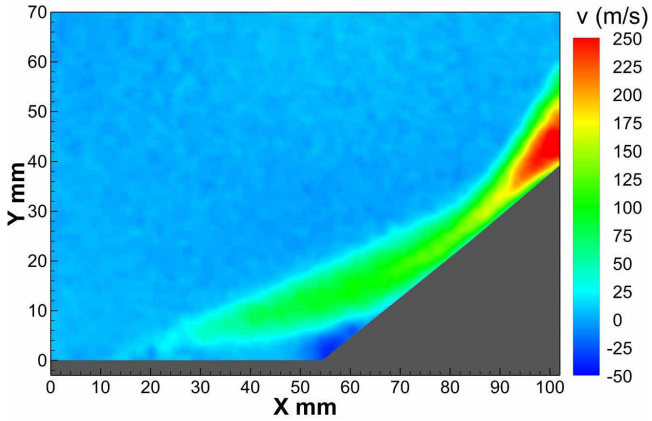

(d) Longitudinal velocity contours

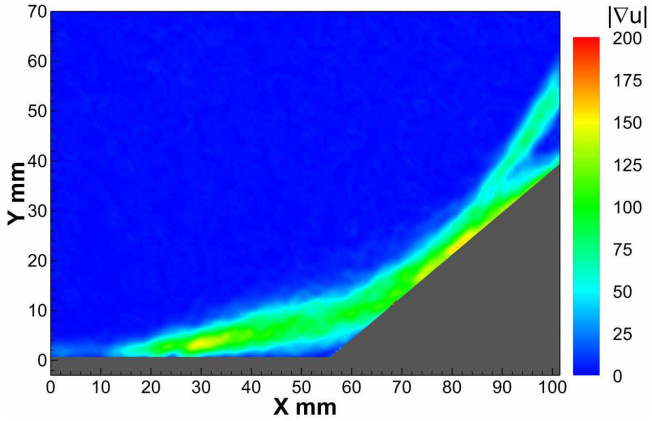

(e) Gradient contours of the streamwise velocity

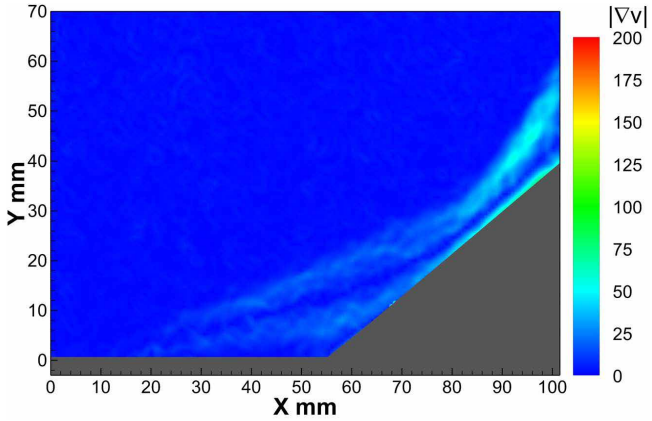

(f) Gradient contours of the longitudinal velocity

Figure 6: PIV measurement results of the 36° compression ramp model.

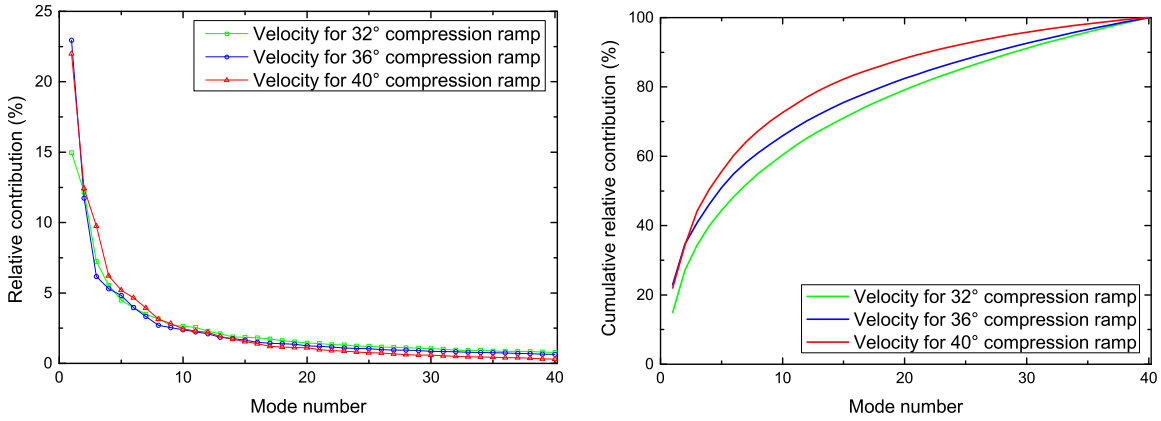

(a) Relative contribution of individual POD modes

(b) Cumulative relative contribution

Figure 7: POD analysis results for the three different compression ramps.

efficiently it is represented by the POD expansion. The contributions from the other modes decrease very quickly with increasing mode number, especially for large ramp angle cases. For cumulative contributions, the case for the velocity of a large ramp angle converges slightly faster than that for the small ramp cases. The results show that the level of coherency for the large compression ramp angle is higher than that for the small compression ramp cases.

4 Conclusion

Due to the interaction of the shock wave with the boundary layer and the interaction of the shock wave with itself, the flow field of the compression ramp includes complex flow field structures such as separation, s-hearing and reattachment. This condition may cause high-frequency pulsations of the aircraft's aerodynamic forces, surface heat flow and pressure loads and cause structural damage to the aircraft. The aims of this research project are to measure the velocity fields of the hypersonic laminar flow over compression ramps by PIV and analyze the effects of different ramp angles on the flow separation. Experimental investigations of hypersonic laminar flow over a compression ramp are carried out in a Mach 5.0 wind tunnel, and the angles of ramp are 32°, 36° and 40°. High-spatial-resolution images of the laminar inflow over the three different compression ramps are captured. The fine structures of the holistic flow field and local regions are measured by the PIV technique, and some typical flow structures, such as the boundary layer, shear layer, separation shock, recirculation zone and reattachment shock, are clearly visible. POD analysis of velocity fields is performed for three cases and reveals the spatial structure characteristics of the flow field.

The experimental results indicate that when the ramp angle is 32°, the hypersonic laminar flow does not show separation, and the boundary layer always adheres to the ramp. When the ramp angle increases to 36°, a typical separation appearing in the hypersonic laminar flow with boundary layer increases and is converted into turbulence quickly; at the same time, a shock is induced by the developing boundary layer, and shear layer and compression waves arise in the flow field. When the ramp angle is 40°, the range of the recirculation zone expands obviously in the hypersonic laminar flow which is separated further, the separation shock moves upstream, and the reattachment shock moves downstream. The POD analysis results indicate that the ratio of the turbulent kinetic energy for a large compression ramp angle is larger than that for a small compression ramp angle. The level of coherency for the large compression ramp angle is higher than that for the small compression ramp cases.

Acknowledgements

The author thanks the Hypervelocity Aerodynamics Institute of China Aerodynamics Research and Development Center for providing the experimental site and for permission to release the experimental results. This work was supported by the National Natural Science Foundation of China under Grant 51875228 and Grant 51475193.

References

Agostini L, Larchevêque L, and Dupont P (2015) Mechanism of shock unsteadiness in separated shock/boundary-layer interactions. *Physics of Fluids* 27:126103

Chatterjee A (2000) An introduction to the proper orthogonal decomposition. *Current science* 78:808–817

Edwards JR, Choi JI, and Boles JA (2008) Large eddy/reynolds-averaged navier-stokes simulation of a mach 5 compression-corner interaction. *AIAA journal* 46:977–991

Gaitonde DV (2013) Progress in shock wave/boundary layer interactions. in *43rd AIAA Fluid Dynamics Conference, San Diego, California, USA, June 24-27*

Gaitonde DV (2015) Progress in shock wave/boundary layer interactions. *Progress in Aerospace Sciences* 72:80–99

Ganapathisubramani B, Clemens NT, and Dolling DS (2006) Planar imaging measurements to study the effect of spanwise structure of upstream turbulent boundary layer on shock induced separation. in *44th AIAA Aerospace Sciences Meeting and Exhibit, Reno, Nevada, USA, January 9-12*

Ganapathisubramani B, Clemens NT, and Dolling DS (2007) Effects of upstream boundary layer on the unsteadiness of shock-induced separation. *Journal of Fluid Mechanics* 585:369–394

Hadjadj A and Dussauge JP (2009) Shock wave boundary layer interaction. *Shock Waves* 19:449–452

Helmer DB, Campo LM, and Eaton JK (2012) Three-dimensional features of a Mach 2.1 shock/boundary layer interaction. *Experiments in fluids* 53:1347–1368

John B and Kulkarni V (2014) Numerical assessment of correlations for shock wave boundary layer interaction. *Computers & Fluids* 90:42–50

Lee Y, Yang H, and Yin Z (2017a) Outlier detection for particle image velocimetry data using a locally estimated noise variance. *Measurement Science and Technology* 28:035301

Lee Y, Yang H, and Yin Z (2017b) PIV-DCNN: cascaded deep convolutional neural networks for particle image velocimetry. *Experiments in Fluids* 58:171

Podvin B and Fraigneau Y (2017) A few thoughts on proper orthogonal decomposition in turbulence. *Physics of Fluids* 29:020709

Rowley CW (2005) Model reduction for fluids, using balanced proper orthogonal decomposition. *International Journal of Bifurcation and Chaos* 15:997–1013

Schreyer AM, Sahoo D, and Smits A (2011) Turbulence Measurements with PIV in a Hypersonic Shock Boundary Layer Interaction. in *41st AIAA Fluid Dynamics Conference and Exhibit, Honolulu, Hawaii, USA, June 27-30*

Sieber M, Paschereit CO, and Oberleithner K (2016) Spectral proper orthogonal decomposition. *Journal of Fluid Mechanics* 792:798–828

Wu M and Martin MP (2008) Analysis of shock motion in shockwave and turbulent boundary layer interaction using direct numerical simulation data. *Journal of Fluid Mechanics* 594:71–83

Zhong Q, Yang H, and Yin Z (2017) An optical flow algorithm based on gradient constancy assumption for PIV image processing. *Measurement Science and Technology* 28:055208